The Astronomical Journal, 136:1312–1324, 2008 September doi:10.1088/0004-6256/136/3/1312

SPATIAL EXTENSION IN THE ULTRAVIOLET SPECTRUM OF VV CEPHEI

Wendy Hagen Bauer[1], Theodore R. Gull[2], and Philip D. Bennett[3,4]
[1] Whitin Observatory, Wellesley College, 106 Central St., Wellesley, MA 02481, USA; wbauer@wellesley.edu
[2] Code 667, Astrophysics Science Division, NASA Goddard Space Flight Center, Greenbelt, MD 20771, USA; Theodore.R.Gull@nasa.gov
[3] Eureka Scientific, Inc., 2452 Delmer Street, Suite 100, Oakland, CA 94602, USA
[4] Department of Astronomy & Physics, Saint Mary's University, Halifax, NS B3H 3C3, Canada; pbennett@ap.stmarys.ca
Received 2008 April 5; accepted 2008 June 14; published 2008 August 15

ABSTRACT

Two-dimensional processing of *Hubble Space Telescope*/Space Telescope Imaging Spectrograph (*HST*/STIS) echelle spectra of the eclipsing M2 Iab + B binary system, VV Cep, has revealed extended emission in all 21 epochs observed, ranging from midtotality through the first quadrature. In the ultraviolet accessible to STIS (1150–3150 Å), essentially all observed photons originate from the hot component. In total eclipse, a pure emission spectrum is seen, with strong lines from lower levels up to ∼2 eV cut by blue-shifted absorption in the M supergiant wind. Out of eclipse, a continuum is observed upon which a rich absorption spectrum of mostly neutral and singly-ionized iron group elements is superimposed. Out of eclipse, the strongest absorption features sit atop the emission profiles seen during eclipse. Far from eclipse, the neutral lines disappear, and the strongest of the remaining absorption lines develop complex inverse P-Cygni profiles. The continuum and spectrally extended blue wings of the inverse P-Cygni spectral lines show a spatial extension characteristic of the *HST*/STIS response to an unresolved source. However, the emission components of spectral lines lying longward of the blue-shifted wind absorption typically show flux extending beyond the unresolved hot component, implying formation over an extended region much larger than the size of the binary orbit. This extended line emission is believed to be formed by scattering of photons from the hot component's continuum by ions in ground and low-lying metastable levels in the extended wind of the M supergiant. Extension is observed out of eclipse for lines with lower levels up to approximately 4 eV, but the greatest degree of extension is observed for lines with lower levels less than 2 eV. Radial velocity differences across the spatially extended emission correlate with the aperture position angle, consistent with model predictions for wind flow in a binary system in which the wind outflow is comparable to the orbital velocity, and indicate an orbital plane oriented from +11° E of N (receding) through −169° (approaching).

Key words: binaries: close – stars: individual (VV Cep) – stars: winds, outflows – ultraviolet: stars

Online-only material: color figures

1. INTRODUCTION

Despite decades of effort, the acceleration mechanism for red supergiant winds is not yet understood. Unfortunately, most observations are unable to spatially resolve the structure in the winds. Eclipsing binary systems containing a cool, evolved star (undergoing mass loss via a massive stellar wind) and a hotter, more compact main-sequence companion provide us with the opportunity to derive information about the spatial structure within the extended cool star chromosphere and wind. As the hot companion enters and emerges from eclipse, it provides a source of continuous radiation that can be used to probe the extended atmosphere and wind of the late-type primary. The orbital motion allows us to probe different parts of the cool star atmosphere through the varying amount of absorption along the line of sight to the hot star. These observations are particularly useful in the ultraviolet (UV), where the radiation from the hot component dominates the spectrum, thereby avoiding the complexities of dealing with a composite spectrum.

The VV Cephei (=HR 8383 =HD 208816) is an M2 Iab supergiant with a hot companion, probably an early B-type main-sequence star. The orbital period is 20.3 years, with total eclipse lasting about a year and a half. While the system was observed extensively with the *International Ultraviolet Explorer* (*IUE*) satellite over nearly a full orbit (Hagen et al. 1980; Hack et al. 1989; Bauer et al. 1991; Bauer & Bennett 2000), no data were collected during total eclipse. Absorption lines of neutral elements and singly-ionized elements with low ionization potentials (e.g., Ti II and V II) disappeared or weakened considerably as the hot component emerged from eclipse. However, absorption from most singly-ionized elements persisted throughout the orbit, frequently with variable line profiles. Sharp absorption lines originating from low-lying energy levels ($\lesssim 2$ eV) were observed throughout the orbit, blue-shifted by $\sim$20 km s^{-1} from the systemic velocity and remaining invariant with the orbital phase. This absorption presumably forms in the M supergiant wind in a region with spatial extension well beyond the orbit of the hot companion.

The first UV observations of the system during total eclipse were made in 1997 with the *Hubble Space Telescope* Space Telescope Imaging Spectrograph (*HST*/STIS). Bennett et al. (2002) present a review of the VV Cep binary system and the use of eclipsing binaries for mapping the extended atmospheres and winds of red supergiants, and show some early results from the *HST*/STIS observational program. VV Cephei was observed with STIS at a total of 21 epochs during and after the 1997–98 eclipse, through the first quadrature in 2003. Table 1 summarizes these observations. High (E230H) and medium resolution (E230M) echelle observations were obtained in the near ultraviolet (NUV) at each observation epoch. Medium resolution (E140M) echelle observations of the far ultraviolet (FUV) spectrum were also obtained for most epochs, and high-resolution (E140H) FUV observations were obtained for about half of the epochs. One-dimensional extracted spectra

Table 1
HST Observations of VV Cep

Epoch	Midobservation Date (UT)	GO Program	Position Angle (degrees)	Orbital Phase
1	1997 Nov 29.26	GO-7269/Visit 1	30	0.9897
2	1998 Mar 21.98	GO-7269/Visit 2	−80	0.0049
3	1998 Jul 14.63	GO-7269/Visit 5	168	0.0203
4	1998 Aug 1.40	GO-7269/Visit 4	152	0.0227
5	1998 Aug 20.04	GO-7269/Visit 6	135	0.0252
6	1998 Sep 8.45	GO-7269/Visit 7	117	0.0279
7	1998 Sep 23.19	GO-7269/Visit 8	101	0.0298
8	1998 Oct 13.88	GO-7269/Visit 53	79	0.0326
9	1998 Nov 1.42	GO-7269/Visit 9	59	0.0351
10	1998 Dec 1.94	GO-7269/Visit 10	27	0.0392
11	1998 Dec 29.15	GO-7269/Visit 11	1	0.0429
12	1999 Feb 23.02	GO-7269/Visit 12	−52	0.0504
13	1999 Apr 20.76	GO-7269/Visit 13	−112	0.0580
14	1999 Jun 16.87	GO-7269/Visit 14	−168	0.0657
15	1999 Aug 12.49	GO-8257/Visit 1	147	0.0733
16	2000 May 18.74	GO-8257/Visit 2	−138	0.1111
17	2000 Sep 7.41	GO-8779/Visit 1	117	0.1261
18	2001 Feb 22.31	GO-8779/Visit 2	−48	0.1487
19	2001 Aug 8.46	GO-9231/Visit 1	146	0.1712
20	2002 Sep 2.42	GO-9231/Visit 2	132	0.2237
21	2003 Sep 25.38	GO-9231/Visit 12	99	0.2759

show behavior consistent with the *IUE* observations, and will be discussed more fully by P. D. Bennett et al. (2009, in preparation). Following the successes of STIS at detecting an extended structure in objects such as η Car (cf. Gull et al. 2006), the spectra were reprocessed in two dimensions using High Resolution Echelle Spectrometer (HIRES) pixels with a spatial extent of 0.″0145, which corresponds to ∼4.5 M supergiant radii. Spatially extended emission was detected at all 21 epochs.

2. THE SYSTEM AND THE ONE-DIMENSIONAL SPECTRA

The orbit of the hot component relative to the M star as seen projected on the sky is shown in Figure 1. Radial velocity observations by Wright (1977) determined the scale of the orbit in AU and masses of ∼20 $M_\odot$ for both stars. A major problem in determining the secondary orbit is the lack of obvious absorption features from the hot star. A significant fraction of the companion's UV spectrum is evidently nonstellar, variable Balmer continuum emission. Balmer line emission and the Balmer jump (also in emission) are prominent when the Balmer continuum is high, with Balmer lines present in emission to about H-16 at $\phi = 0.1712$ (near the first quadrature), as observed by the STIS/G430L low-resolution grating spectrograph. Wright avoided the lack of intrinsic hot star absorption by deriving a radial velocity for the hot component from the prominent Hα emission. Although the radial velocity curve for this emission is in the opposite sense of that for the M star, the emission may not be centered on the hot component but instead may be biased toward an interaction region between the two stars where the excitation of Balmer radiation is maximal. This scenario would likely result in a smaller observed radial velocity amplitude for the Hα emission compared to a photospheric line of the companion star. Consequently, the mass of the secondary star determined from Hα radial velocities may be overestimated.

The angular diameter of the M supergiant (6.38 mas) was derived from fits of *RIJHKL* and *Infrared Astronomical Satellite*

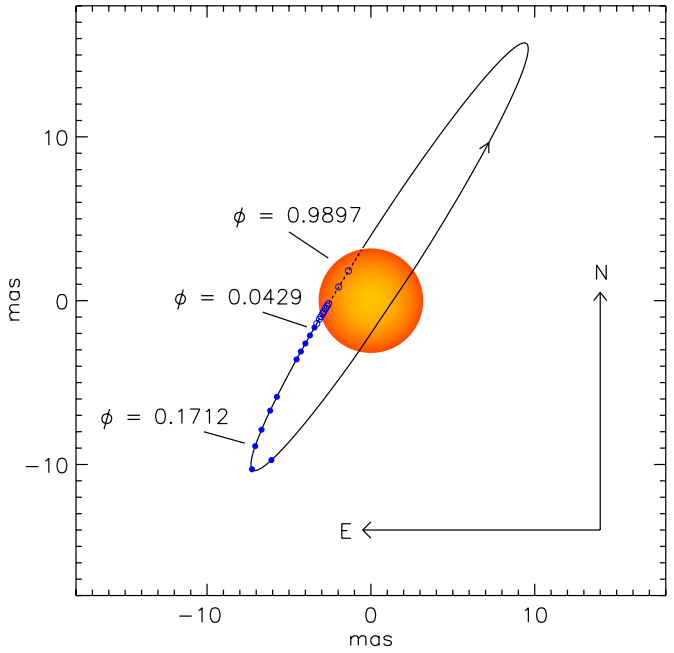

Figure 1. The orbit of VV Cephei, as seen projected on the sky. The relative orbit of the hot component and its position at the times of the *HST* observations are plotted. The size of the M supergiant is to scale, based on emergence from eclipse at visible wavelengths. The filled circles are the observations for which the hot component's continuum had fully emerged in the NUV (longward of ∼1600 Å). A few of the observations discussed in the text have been annotated. The lengths of the arrows labeling the north and east directions are the size of the HIRES pixels in the spatial direction.

(A color version of this figure is available in the online journal.)

(*IRAS*) 12 μm band photometry (bands where the hot companion contributes negligible flux), reddened by interstellar extinction of $A_V = 1.24$, to the spectral energy distribution of an M2 supergiant from models of Lejeune et al. (1997). The extinction was derived from $E(B - V) = 0.4$ of Hack et al. (1989), adopting the usual value of $R_V = A_V/E(B - V) = 3.1$ appropriate to the diffuse interstellar medium, and using the formula of Cardelli et al. (1988) to compute A_λ. Eclipse timings (primarily of second and third contacts) constrain the length of the eclipse chord. Together with the spectroscopic orbit solution of Wright (1977), a complete solution of the orbital and stellar parameters of the VV Cep binary is obtained, including a reasonable constraint on the inclination angle (84°), the M supergiant's radius (1050 $R_\odot$ at optical wavelengths), and the binary's distance (1.5 kpc). The solution method follows that of Bennett et al. (2004); an updated version of this analysis is given by P. D. Bennett (2009, in preparation). The orientation of the orbit on the plane of the sky used the astrometric orbit (in particular, the position angle of the ascending node: $\Omega = 147°$) of van de Kamp (1977), derived from decades of long-focus astrometry of the binary photocenter at Sproul Observatory.

During the first nine *HST* observations of VV Cep, the eclipse was total in the UV. A rich emission spectrum was observed. Bauer et al. (2007) describe this spectrum in detail and provide an atlas with identifications for the ∼2000 emission features seen during totality. Emission from strong low-excitation[5] lines (up to ∼2 eV) is cut by sharp absorption blue-shifted by

[5] In this paper, the excitation of a transition refers to the lower-energy level of the transition leading to the line in question. Hence a low-excitation transition refers to absorption from or emission leading to an energy level typically less than 2 eV and a high-excitation transition refers to absorption from or emission leading to an energy level typically greater than 3 eV.

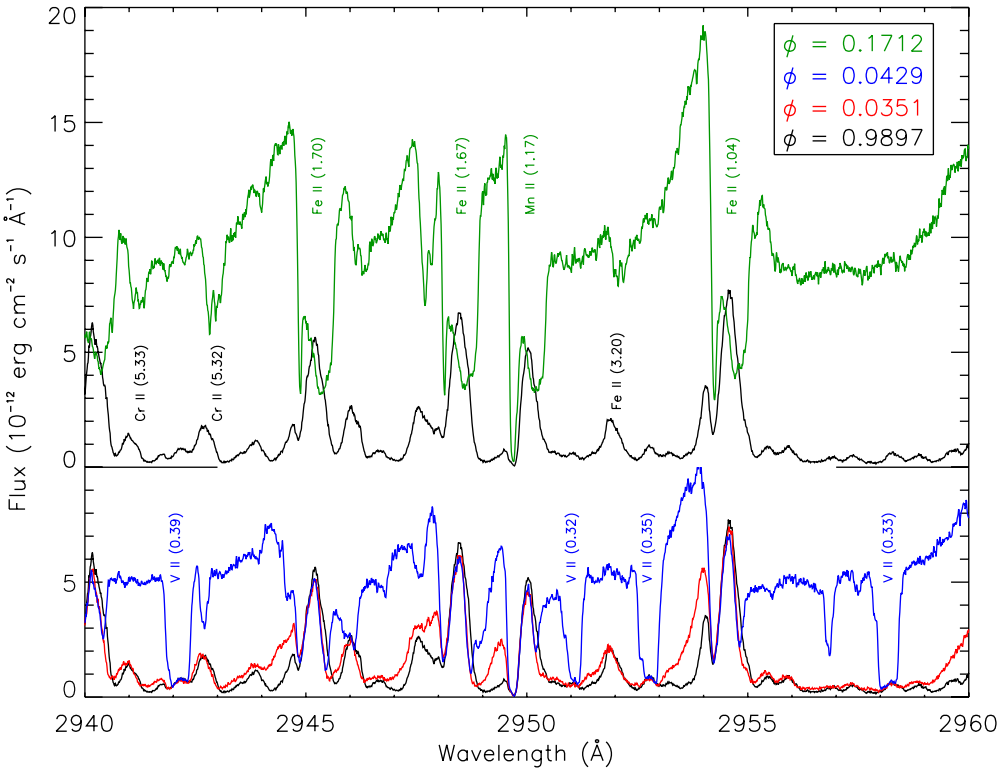

Figure 2. The temporal evolution of the spectrum. In the lower portion of the figure, observations made on 1997 November 29 ($\phi = 0.9897$, near midtotality) and 1998 November 1 ($\phi = 0.0351$, just before egress in the near-UV) are compared to observations made on 1998 December 29 ($\phi = 0.0429$, just after egress in the NUV). Note the brightening of the short-wavelength edges of emission features between midtotality and just before egress, and how strong absorption just after egress bottoms out on the emission seen during totality. Strong lines of V II have been annotated in blue and labeled with their lower-energy level in eV. In the upper portion of the figure, the midtotality spectrum is replotted and compared with observations made on 2001 August 8 ($\phi = 0.1712$, near the first quadrature). Note that the V II absorption has disappeared. By this time, only the strongest absorption still bottoms out on the emission seen during eclipse. Some of these absorption features are annotated in green. There has also been some Doppler shifting in the emission, but note that the sharp blue-shifted wind absorption features do not shift. Some weaker lines transitioning down to higher-energy levels that are seen in emission during totality but in absorption out of eclipse are annotated in black.

$\sim$20 km s^{-1} relative to the systemic velocity, consistent with wind absorption features observed in optical spectra. Weaker and higher excitation lines show fairly symmetric emission profiles near midtotality. As egress of the hot stellar companion from eclipse approached, emission systematically strengthened on the short-wavelength side of the line profile, as seen in the lower panel of Figure 2. The gradual emergence of this blue-shifted emission just prior to the egress of the hot star's continuum implies that it arises from an emitting region closely associated with, but several times larger than, the hot stellar companion.

Temporal changes in the spectrum are presented in detail in P. D. Bennett et al. (2009, in preparation) and summarized in Figure 2. Once the hot component emerges from eclipse, it provides a UV continuum and the nature of the spectrum changes to one dominated by absorption. Absorptions from neutral elements and singly-ionized elements with low ionization potentials (such as Ti II and V II) weaken systematically and dramatically as egress progresses. Presumably, this is a consequence of increasing photoionization of these easily-ionized species by the companion's FUV continuum as the line of sight through the chromosphere becomes optically thin in the respective bound-free continua. For example, the strong V II absorption seen in Figure 2 at $\phi = 0.0429$ (the first observation made after the hot component had fully emerged in the NUV) is gone by $\phi = 0.1712$ (near the first quadrature). In contrast, absorption due to singly-ionized elements with higher ionization potential persists throughout the orbit, often with prominent inverse P-Cygni profiles in strong lines. This is seen in the Fe II and Mn II 1–2 eV lines plotted in Figure 2. Right after totality ends, absorption from strong lines bottoms out directly on the emission observed during totality, which suggests that the underlying emission comes from a more extended volume than does the absorption. By the first quadrature, strong absorption still appears to bottom out on underlying emission, although the emission has been Doppler shifted. This behavior suggests a model in which the UV emission observed during totality comes from line photons scattered by an extended circumstellar shell or wind. The blue-shifted absorption feature near -20 km s^{-1} (systemic) persists throughout the orbit, suggesting a source in the foreground stellar wind near terminal velocity.

3. THE SPATIALLY RESOLVED SPECTRA

The data shown in Figure 2 were extracted and reduced by the standard CALSTIS software producing one-dimensional spectra (Valenti et al. 2002). The extracted spectra were coadded to form a continuous one-dimensional spectrum over the entire range of each of the E230H, E230M, and (when observed) E140M and E140H echelles. The coadded spectra were independently flux-calibrated by normalizing to low-resolution G230LB/G430L spectra observed through a photometric aperture. Considerable effort was devoted to removing artifacts originating from the ends of echelle orders from the coadded spectrum.

The data shown in Figure 3 and subsequent plots were reprocessed with a modified IDL version of this routine to extract spatially-resolved row-by-row spectra at the 0.″0145 spatial HIRES pixel sampling. The spatially-resolved spectra presented

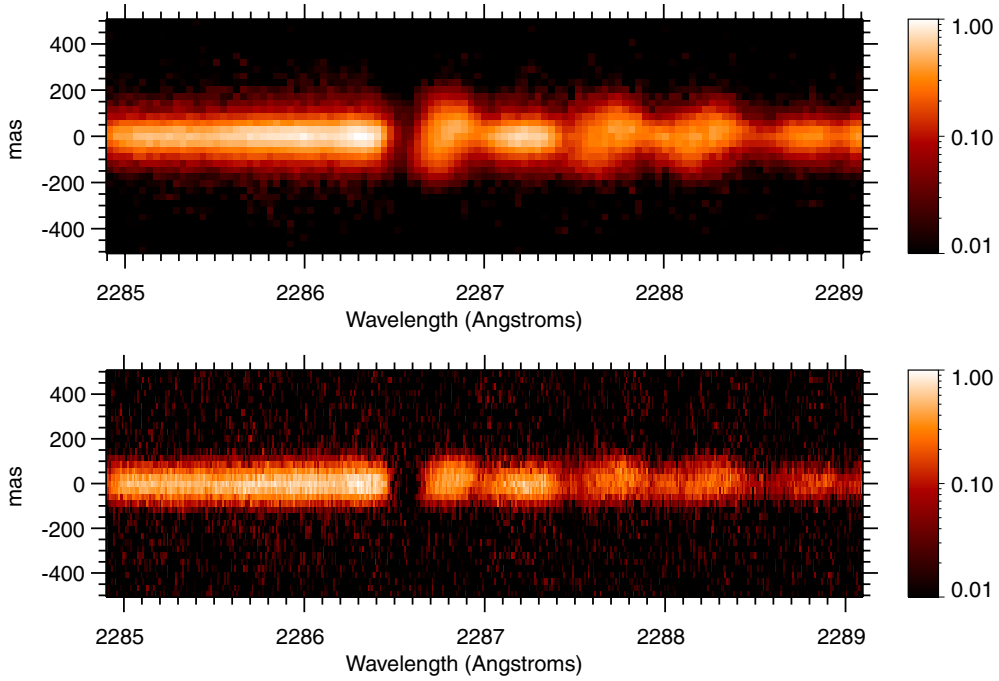

Figure 3. The two-dimensional spectral displays. These observations were made at $\phi = 0.0429$ (1998 December 29), just after egress from eclipse, with aperture position angle +1°. The observations in the upper panel were made at medium spectral resolution, with a 0.″2 × 0.″2 aperture, while those in the lower panel were made at high spectral resolution with an 0.″1 × 0.″2 aperture. Emissions near 2286.8, 2287.6, and 2288.2 Å are seen to be more spatially extended than the rest of the spectrum, particularly in the upper panel. The smaller aperture used for the observations in the lower panel occults some of the extended emission.

in this paper have not been corrected for intensity variation along the echelle orders, and hence are not flux-calibrated. However, over the narrow wavelength ranges considered in this paper, the "relative flux" extracted from these HIRES pixels is quantitatively useful for investigating the spatial distribution of flux within a given spectral line profile.

Figure 3 depicts two-dimensional representations of a selected portion of two spectra observed at $\phi = 0.0429$, just after the hot component's continuum had emerged from eclipse. The data in the upper panel were taken at medium spectral resolution (E230M) through the 0.″2 × 0.″2 aperture, and the data in the lower panel were taken at high spectral resolution (E230H) through the 0.″1 × 0.″2 aperture. Note that the difference in apertures (0.″1 versus 0.″2) is along the spatial direction of the spatially-resolved spectra. The strong absorption feature near 2286.5 Å is the blue-shifted wind absorption component (−20 km s^{-1} systemic) from a strong line of Co II originating from the 0.42 eV level. This line behaves like the strong low-excitation Fe II and Mn II lines plotted in Figure 2, showing an inverse P-Cygni profile and with strong, optically thick, absorption out of eclipse bottoming out on wind emission that was visible during totality. This wind emission, seen near 2286.7 Å in Figure 3, is clearly more spatially extended than the regions of the spectrum from 2285 to 2286.4 Å and 2287.2 to 2287.4 Å. Extended wind emission is also seen near 2287.7 and 2282.2 Å (from Ni II 1.86 and 3.10 eV). Comparison of these two observations clearly shows that the smaller aperture occults the extended emission. As will be discussed in Section 4, there is an obvious radial velocity difference between the wind emission seen above and below the center of the spectrum in this observation.

The two plots on the left side of Figure 4 depict the size of these two apertures relative to the HIRES pixel sizes, and include the angular size of the M supergiant and the extent and orientation of the orbit. These diagrams show the system in the aperture as it would appear when the detector and aperture have a position angle of 0°. At this position angle, the spatial extension (increasing detector row number) points due north. Positive position angles correspond to rotating the aperture counter-clockwise or eastward from north.

The STIS echelle observations as shown in Figure 3 were made when the position angle of the aperture was +1°, almost exactly the same as the orientation of the aperture and pixels as depicted on the left side of Figure 4. The panels on the right side of Figure 4 quantify the data displayed in Figure 3. The black line in these spectral plots is the relative flux extracted from the central row of spatial pixels, and the colored lines are the spectra extracted moving one row away at a time. In these two images, the rows plotted are those above the central row in the aperture diagrams (left) and step to the north of the central row. In this paper, "above" the central row will refer to an increasing detector row number. The relevant position on the sky depends on the aperture/detector position angle.

During eclipse, emission presumably due to the M supergiant wind was visible in the features near 2286.7, 2287.7, and 2288.3 Å but most of the flux shortward of 2286 Å and near 2287.2 Å did not appear until the hot component emerged from eclipse, and is thus physically associated with it, either as continuum or as inverse P-Cygni emission. The greater spatial extension of the wind emission features as compared to regions of P-Cygni emission and continuum can be seen in these plots by how much more rapidly the relative flux falls off away from the central row. Note in particular the red line, which plots two rows (0.″029) away from the central row: it is nearly as strong as the central row in the wind emission features but only about half as strong in the continuum and inverse P-Cygni regions.

As can be seen in Figure 3, the larger 0.″2 × 0.″2 aperture permits the detection of extended emission farther from the

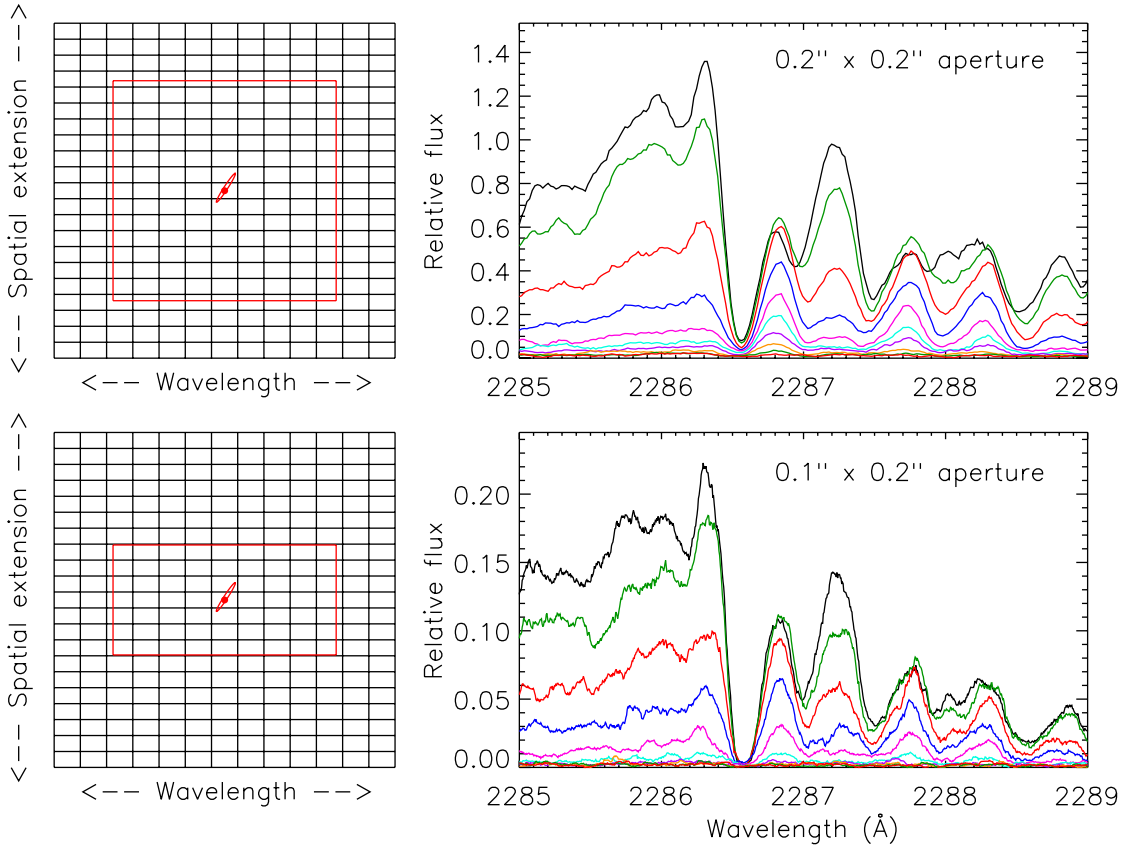

Figure 4. Aperture sizes and row-by-row spectral plots. The left side of the figure shows the sizes of the HIRES pixels and the apertures relative to the scale of the M supergiant and the relative orbit of the hot component, for an aperture position angle of 0°. The right side of the figure shows data observed from these configurations on 1998 December 29 ($\phi = 0.0429$), just after egress from eclipse, which was observed at an aperture position angle of +1°. The black line is the relative flux extracted from the central row of pixels and the colored lines plot the flux extracted from the rows of pixels above the central row, as seen in the left side of the figure (which was to the north in this observation). Note how the flux in the wind emission from Co II seen near 2286.8 Å falls off less rapidly away from the central row than it does from the regions of continuum seen near 2287.2 Å or shortward of 2286.2 Å, especially in the larger aperture. The data taken through the 0.″2 × 0.″2 aperture were obtained at medium spectral resolution and those through the 0.″1 × 0.″2 aperture at high spectral resolution.

central row than does the 0.″1 × 0.″2 aperture. The relative flux from the sixth row away from the central row is plotted in violet, and the wind emission is clearly detected in this row through the 0.″2 × 0.″2 aperture but not at all with the 0.″1 × 0.″2 aperture. The reader may notice that some emission appears beyond the projected aperture height (e.g., the fourth row, 0.″058 beyond the central row). This is simply due to the broad response of the point spread function (PSF) of the STIS spectrograph and Multianode Microchannel Array (MAMA) detector to the extended wind emission out to the edge of the 0.″1 high aperture. Likewise, some extension is seen in the eighth row (0.″116) of the 0.″2 aperture.

One way to demonstrate that these emission lines are spatially extended is by comparison to the spatial PSF of the *HST*/STIS echelle configurations. As noted in the STIS Instrument Handbook (Quijano et al. 2007), the LSFs for these configurations are about 1.7 LORES or 3.4 HIRES pixels full width at half-maximum (FWHM), which equals ∼0.″049. However, both long-term and short-term focus drifts can result in less than optimal spatial resolution. Direct measure of echelle spectra of standard stars yielded FWHM measures of approximately 0.″060, being somewhat poorer than optimal in the NUV. However, the spectra recorded of VV Cep have internal measures of relevance to this question which is of great importance due to potential focus drifts.

The continuum recorded in these echelle spectra orginates primarily from a region closely associated with the hot component in the spatial direction. As we already noted, the wind lines originate from a spatially larger region; we present an example in Figure 5 using the data already presented in Figures 3 and 4. The relative fluxes in each row were summed up for a specific wavelength interval and then normalized to unity for the row with the most flux. We compare in Figure 5 the normalized spatial profile for flux believed to be associated with the hot component to the normalized spatial profile of the wind emission in the 2286.86 Å line of Co II. The greater extension in the Co II line relative to the continuum is immediately apparent. Measures for several lines depicted in Figure 4 are summarized in Table 2. The FWHM from regions that arise

Table 2
FWHM of Line and Continuum[a] Regions

Ion	χ (eV)	Wavelength (Å)	Wavelength Region (Å)	FWHM (arcsec) 0.″2 × 0.″2	FWHM (arcsec) 0.″1 × 0.″2
Co II	0.42	2286.86	2286.6–2286.9	0.109	0.073
Ni II	1.86	2287.79	2287.5–2287.9	0.099	0.074
Ni II	3.10	2288.35	2288.0–2288.5	0.085	0.069
Continuum			2285.2–2286.3	0.059	0.058
Continuum			2287.0–2287.4	0.060	0.057

Notes. This table was prepared using observations made at $\phi = 0.0429$ (1998 December 29).
[a] The 2285.2–2286.3 Å spectral region also includes some inverse P-Cygni emission in the blue wing of the Co II line.

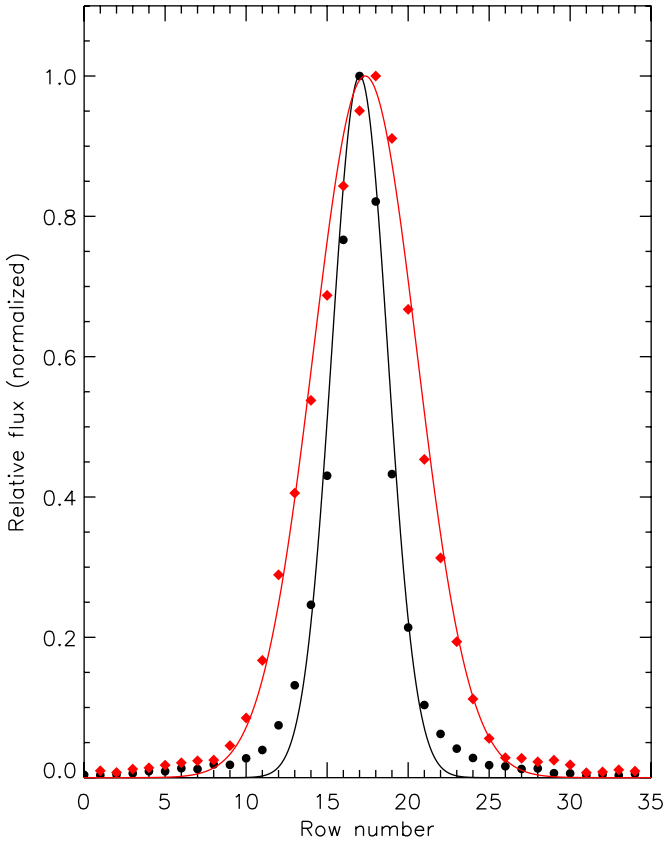

Figure 5. The relative spatial distribution of flux. Filled circles and diamonds represent the sum of the relative flux in each row within a given wavelength region, normalized to the row with the greatest value. The scale is 0.″0145/row. The solid lines are Gaussian fits to the data. The observations of 1998 December 29, $\phi = 0.0429$ with the 0.″2 × 0.″2 aperture presented in Figure 4 were used. Results from 2285.4–2286.5 Å are plotted with filled circles and results from 2286.8–2287.1 Å are plotted with diamonds. Most of the flux in the 2285.4–2286.5 Å region did not appear until the hot component had emerged from eclipse, and is believed to form in a region of limited spatial extent around the hot star, which would be unresolved by *HST*/STIS. Therefore, the observed flux distribution across the detector rows in this spectral region should provide an empirical estimate of the STIS spatial PSF. In contrast, the emission between 2286.8 and 2287.1 Å is believed to form in the extended wind of the red supergiant primary, and we expect and observe a flux distribution on the detector, which is significantly broader than the flux physically associated with the hot component.

(A color version of this figure is available in the online journal.)

from wind emission are larger than those that arise from flux physically associated with the hot component.

The referee of this paper inquired whether the shift of the centroid of the Gaussian fit to the wind emission relative to the fit to the flux associated with the hot component is real. At the time of this observation, $\phi = 0.0429$, the position angle of the STIS aperture maximized the radial velocity shift seen above and below the hot component. In this particular case, wind emission below the hot component is blue-shifted enough to be strongly absorbed by the outer wind (see Figure 3). Hence, the effect is indeed real. This behavior is consistently seen in lines with strong blue-shifted wind absorption observed at this epoch.

These two-dimensional observations now permit us to determine whether emission arises from the extended wind of the M supergiant or from a more localized area. We hypothesized that the systematic increase of the emission on the short-wavelength side of line profiles between midtotality and egress shown in Figure 2 arises from gas near the hot component emerging from behind the M supergiant. The spatial distribution of the observed flux shows that this emission indeed arises from a localized volume in space. Medium spectral resolution data taken through the 0.″2 × 0.″2 aperture of the same 0.42 eV Co II line plotted in Figure 4 are shown at three different epochs in Figure 6. In all panels, the black line is the spectrum extracted from the central row, the green line is that from four rows above the central row, and the orange line is that from four rows below. Four rows of HIRES pixels correspond to 0.″058, ∼18 M supergiant radii. In the left panel, which plots $\phi = 0.9897$ (near midtotality), not much difference is seen in the line profile between the central row and the other rows. The central panel presents the last observation before NUV egress ($\phi = 0.0351$), when the short-wavelength peak has brightened as gas near the hot star has emerged. Note the line profile change between the central row and the outer rows. The short-wavelength emission believed to arise from gas near the hot component is not nearly so extended as the emission believed to be produced in the extended wind. The right panel presents observations made at $\phi = 0.0429$, after the continuum has emerged. The greater spatial extension of the wind emission relative to the flux physically associated with the hot component is clearly seen.

While extended emission in the two-dimensional spectra can be seen in plots like Figure 4, it can be more easily detected by making plots like the top panel in Figure 7. Flux from a true point source should have the same spatial PSF at all wavelengths within a given spectral order. Thus, in order to look for extended emission, we summed the relative fluxes in all the HIRES pixels within a given row and normalized the sum to the sum of the relative flux over all rows. After this normalization, spectra extracted from each row of pixels would be expected to lie directly on top of each other if the flux came from a point source. Any increase in flux in the outer rows would be due to other sources in the aperture, or in this case extended wind emission. An example of such a plot is shown in Figure 7 for observations made near the first quadrature. The spectrum extracted from the central row of pixels is plotted in black, with rows above the central row plotted in color. Through most of this wavelength range, the plotted spectra do overlie one another, showing a similar spatial spread. However, two strong 1.17 eV lines of Mn II show significant extra flux off the central row. The other absorption features in this region of the spectrum arise from higher-excitation lines; two unblended Cr II lines are labeled. The lower panel of Figure 7 plots the one-dimensional calibrated spectrum of this region, compared to the spectrum as observed during midtotality. The two Mn II lines are the only ones with deep enough absorption to bottom out onto the emission seen during totality. Examination of the two-dimensional data shows that this is the main criterion for the detection of extended emission in the out-of-eclipse epochs: that a sufficient quantity of the hot star's flux be absorbed, either by material near the hot star or in the line of sight through the M star wind, for the extended emission to be visible.

Table 3 lists elements which show extended emission at $\phi = 0.1712$ (near the first quadrature). For a given ion, the lower the line's excitation potential and the stronger the line's oscillator strength (gf value), the more likely it is to show extended emission. This table includes only lines with wavelengths greater than 2100 Å, due to the broadening of the *HST*/STIS spatial PSF at shorter wavelengths. The lower limit of $\log gf$ to which extension is typically seen is given in Table 3. In some cases, there are too few lines to determine the minimum gf value to within a factor of 10. We annotate these values with

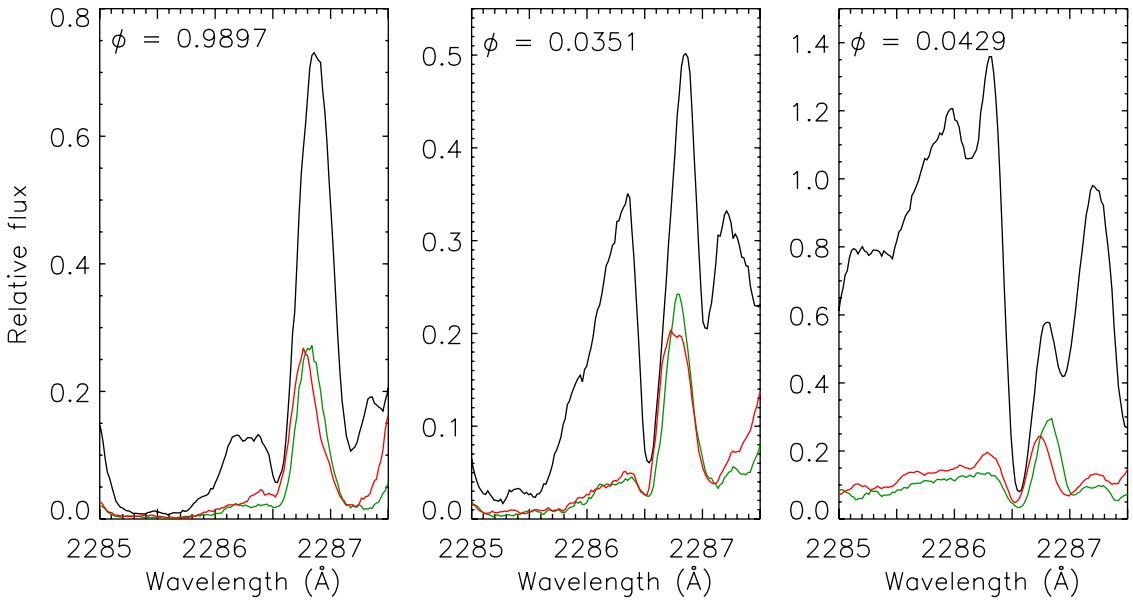

Figure 6. Localizing the emission. The black lines plot the relative flux extracted from the central row of pixels, the green lines plot the relative flux extracted from four rows above the central row, and the red lines plot the relative flux extracted from four rows below, for a wavelength region including a strong 0.42 eV line of Co II. Emission shortward of the wind absorption seen at 2286.5 Å increased from midtotality ($\phi = 0.9897$, 1997 November 29) as gas associated with the hot star approached egress ($\phi = 0.0351$, 1998 November 1). The hot star continuum had fully emerged by $\phi = 0.0429$ (1998 December 29). Note how the emission believed to arise mainly from gas physically near the hot component near and after egress appears much less extended than the emission longward of the wind absorption. The position angles of the aperture during these three observations were +30° ($\phi = 0.9897$), +59° ($\phi = 0.0351$), and +1° ($\phi = 0.0429$). These data were obtained through the 0.″2 × 0.″2 aperture at medium spectral resolution.

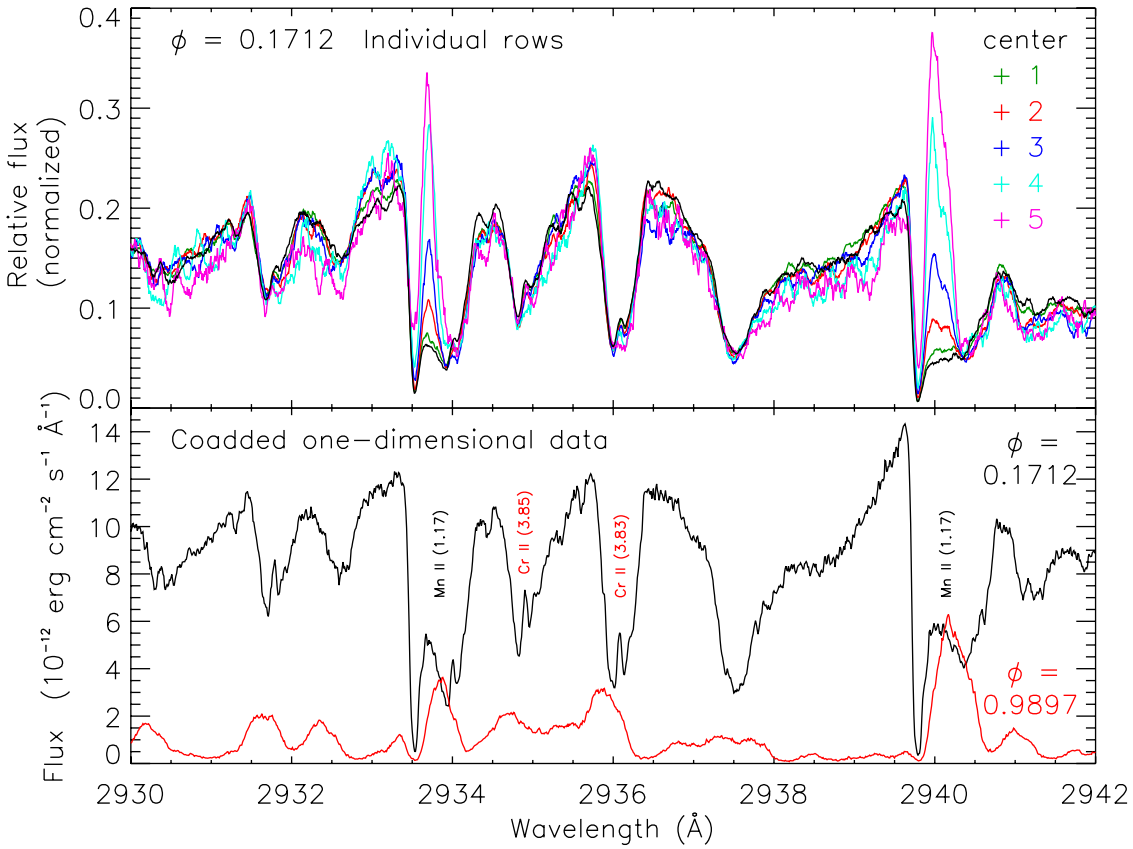

Figure 7. Identifying extended emission. The upper panel plots observations made near the first quadrature ($\phi = 0.1712$, 2001 August 8, position angle +146°). The relative flux in each row is summed and normalized to the sum of the relative flux over all rows. Extended emission shows up as apparent emission above the central row. The lower panel compares one-dimensional extracted and calibrated flux for the first quadrature observation in the upper panel to that observed near midtotality ($\phi = 0.9897$, 1997 November 29). The extended emission seen near the first quadrature appears where the absorption is deep enough to hit emission observed during totality. Some strong lines are labeled with the ion producing them and the excitation potential in eV.

Table 3
Minimum gf Value for Extended Emission Observed Out of Eclipse

Ion	Lower χ (eV)	Minimum log gf
Mg II	0.0–0.0	−0.3:
Ti II	0.0–0.2	−0.6
Cr II	1.4–1.6	−1.0
Cr II	2.4–2.8	−0.5
Mn II	0.0–0.0	0.0:
Mn II	1.1–1.2	0.2:
Fe II	0.0–1.5	−3.0
Fe II	1.5–2.1	−1.0
Fe II	2.1–3.5	−0.5
Fe II	3.5–4.8	0.0
Co II	0.4–1.4	−0.5
Ni II	1.0–1.4	−1.8
Ni II	1.6–1.9	−1.0

Note. This table was prepared using observations made at $\phi = 0.1712$ (2001 August 8).

a colon in Table 3. For the most part, lines that show sharp blue-shifted wind absorption during totality are those for which extension can be detected out of eclipse, with the exception of lines like the 0.00 eV 2852.96 Å line of Mg I with extremely strong interstellar absorption. Spatial extension is observed in the emission peaks of the Mg II h and k lines.

4. DEPENDENCE OF EXTENDED EMISSION ON THE APERTURE POSITION ANGLE

4.1. The Spatial Distribution of Wind Emission

The observations of VV Cep were made with differing aperture position angles. Full exploitation of the resulting capability of mapping the wind emission is beyond the scope of this paper, but we do want to provide one example of the detection of asymmetric emission within the wind. The observations at $\phi = 0.1487$ and 0.1712 were both near the first quadrature, and the observations were made with nearly opposite aperture position angles, −48° and +146° respectively. One would expect that the emission detected in the rows above the central row at $\phi = 0.1487$ should be similar to that detected below the central row at $\phi = 0.1712$ and vice versa. This is indeed what is observed, as is shown in Figure 8. The emission is seen over a narrower range of wavelengths above the central row at $\phi = 0.1712$ and below the central row at $\phi = 0.1487$. This direction corresponds to the SE with a position angle of ∼140°, which is the side of the M star where the B star would be observed at this epoch.

4.2. Radial Velocities

As is seen in Figure 3, some radial velocity structure can be seen in the extended emission. There are noticeable radial velocity shifts between the emission seen above and below the central row of pixels shown in Figure 6. At all three epochs plotted, the emission seen above the central row is red-shifted by varying degrees relative to that seen below the central row.

The interpretation of strong, low-excitation lines is complicated by the presence of the wind absorption components. Figure 9 plots several emission features that do not show wind absorption; the two strongest are the 4.15 and 5.96 eV lines of Fe II at 2238.59 Å and 2239.32 Å respectively. The three epochs plotted are those nearest midtotality, which were observed with very different position angles (annotated on the plots). The orientation of the aperture is depicted above each of the panels. As in Figure 6, the black line plots the spectrum extracted from the central row of pixels, while in this case the green and orange lines represent the spectrum extracted three rows above and below the central row. In the depictions of the aperture orientations, the HIRES pixels in the dispersion directions have been suppressed, while the rows of spatial pixels responsible for the plotted spectra have been outlined in the color in which the spectrum was plotted. Note the opposite radial velocity shifts between the observations at $\phi = 0.9897$ and 0.0203, which have nearly opposite aperture position angles, and that there is a very little radial velocity difference seen at $\phi = 0.0049$.

The radial velocity of emission features seen during totality was measured for each row in the two-dimensional data for lines with high enough excitation to not show wind absorption, yet strong enough to get decent S/N away from the central row, and which were also either unblended or the strongest contributor to a blend. The difference between the radial velocities measured on either side was strongly correlated with the aperture position angle. Figure 10 shows the difference between the velocity measured three rows above the central row and that measured three rows below for a sample of 24 lines measured in high-resolution data taken through the 0.″1 × 0.″2 aperture. Three HIRES pixels correspond to 0.″044 on the sky or ∼14 M-star radii. The error bars are the standard deviation from averaging the results for the 24 lines. The radial velocity was measured from the peak value of a cubic fit to the emission line profile, and a major source of error was the fact that many of the features were somewhat asymmetrical and the fit was determined partly by the actual peak of the emission and partly by the centroid.

A simple sine curve proves to be an excellent fit to the radial velocity differences. This fit is shown as the solid line in Figure 10. The amplitude of this fit is 12.5 km s^{-1}, with an aperture position angle of −79° (and +101°) and a mean radial velocity difference of zero. This is roughly east–west, with most of the northern portion of the envelope moving away from us. The results of the fit to another set of 12 lines observed at medium spectral resolution with the 0.″2 × 0.″2 aperture and for both sets of lines as measured two rows either side of the center were not much different, with amplitudes ranging from 12.7 km s^{-1} to 15.0 km s^{-1} and position angles from −78° to −81°.

Therefore, it appears that we are detecting velocity structure in the wind. The amplitude of the sine curve is comparable to the orbital velocities of the stars; the amplitude of the radial velocity curve for the M supergiant is 19.4 km s^{-1} (Wright 1977). The maximum velocity difference should occur when the orbital plane is oriented perpendicular to the dispersion direction. We find this to be along a line from +11° (just east of north, receding) to −169° (just west of south, approaching), in contrast to the astrometrically determined 147° ascending node (van de Kamp 1977). The portions of the envelope showing red and blue shifts, with similar color coding for the astrometrical binary orbit, are depicted in Figure 11.

This result is supported by hydrodynamical modeling. Several groups have recently performed hydrodynamical studies of wind flows in detached binary systems in which the wind velocity from a mass-losing primary is comparable to the orbital velocity. Theuns & Jorissen (1993), Mastrodemos & Morris (1998), and Gawryszczak et al. (2002) modeled binaries with component masses ∼1 $M_\odot$ in order to model planetary nebular morphology, and all found a spiral flow pattern for the wind. The first two groups present plots of the velocity

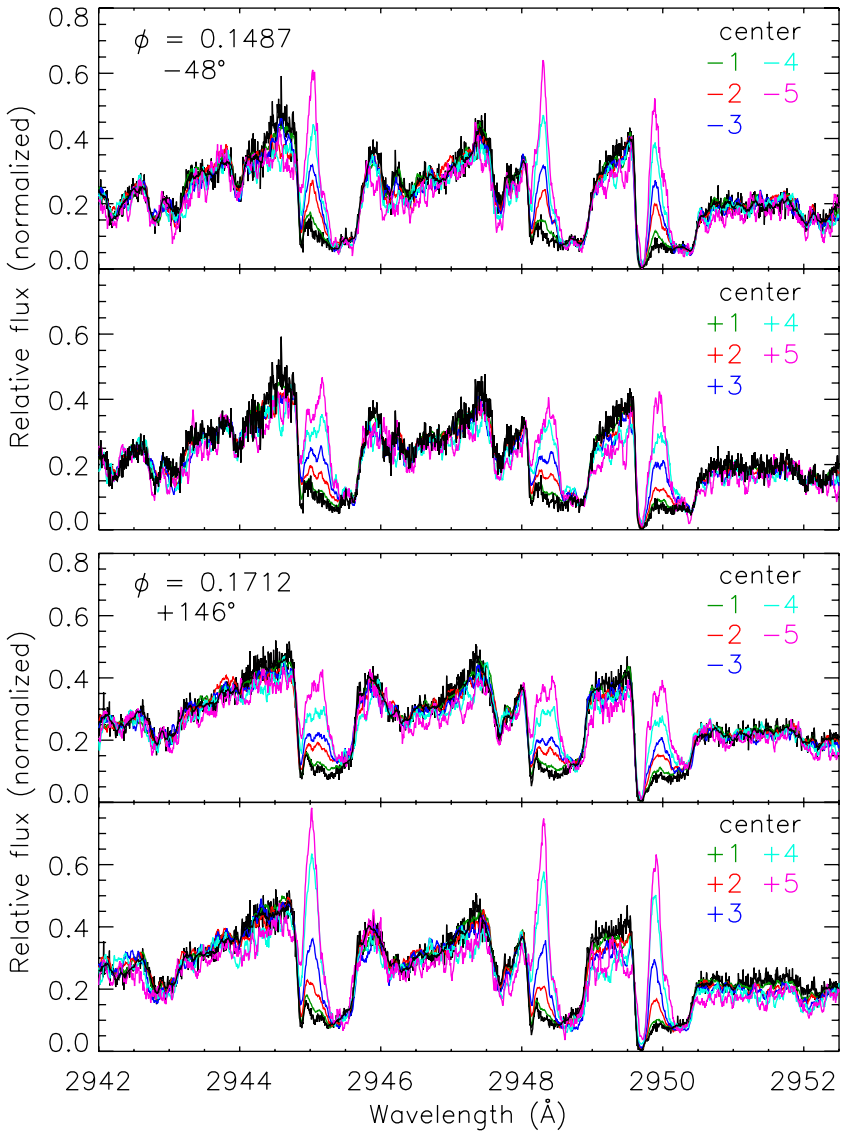

Figure 8. Dependence of observed extension on the position angle. As in the upper panel of Figure 7, relative flux in each row is summed and normalized to the central row. Extended emission is seen in the 2945.26 Å line of Fe II (1.70 eV), the 2948.52 Å line of Fe II (1.67 eV), and the 2950.07 Å line of Mn II (1.17 eV). The aperture position angles (annotated on the figure) were opposite each other at these two epochs, although both observations were made near the first quadrature. The emission above the central row at $\phi = 0.1487$ (2001 February 22) looks similar to that below the central row at $\phi = 0.1712$ (2001 August 8); both were sampling the same region of space (to the northwest). The emission to the southeast also looks similar between the two observations.

structure in the wind flow, and it is clear that the wind retains a significant component of velocity in the direction of the orbital motion. We suggest that this is what we are detecting with our radial velocity measurements. A few studies have also been done for parameters more appropriate to VV Cep. Walder (1997) presented a pioneering simulation of wind accretion for three different cases of well-separated binaries, including a ζ Aur star model (the ζ Aur stars are K supergiant + B star binaries), which would be applicable to VV Cep. More recently, Nagae et al. (2004) computed 3D hydrodynamical models for geometries appropriate to ζ Aur stars, albeit with rather simplified physics. Their models, computed in the frame corotating with the (circular orbit) binary, demonstrate that the flow remains nearly spherical about the mass-losing star, with nearly radial streamlines. In the observer's frame, this flow would have a spiral structure, with the wind retaining much of the rotational and orbital angular momenta. All of these models are broadly consistent, and suggest that the wind of VV Cephei might be expected to show a spiral flow structure.

5. STRENGTH OF THE EXTENDED EMISSION

Fully exploiting the wealth of data would require convolving a model flux distribution with the aperture-dependent PSF, and such an effort is beyond the scope of this paper. We will begin here by making a quantitative estimate of the extended flux at one epoch near the first quadrature, considering only one off-center row, five rows above the center. By five rows away from the central row, the PSF has considerably reduced the contribution from the central row, yet detectable flux remains from lines with extended emission. Five rows of HIRES pixels correspond to 0.″073, or ∼23 M supergiant radii.

In order to get a quantitative value for the extended flux, one must be able to relate the "relative flux" quantity to the extracted and calibrated one-dimensional spectra. The one-dimensional spectral extraction was simulated by adding up the relative flux in the central row and the seven rows on either side of the center for each wavelength element. This allowed us to convert the

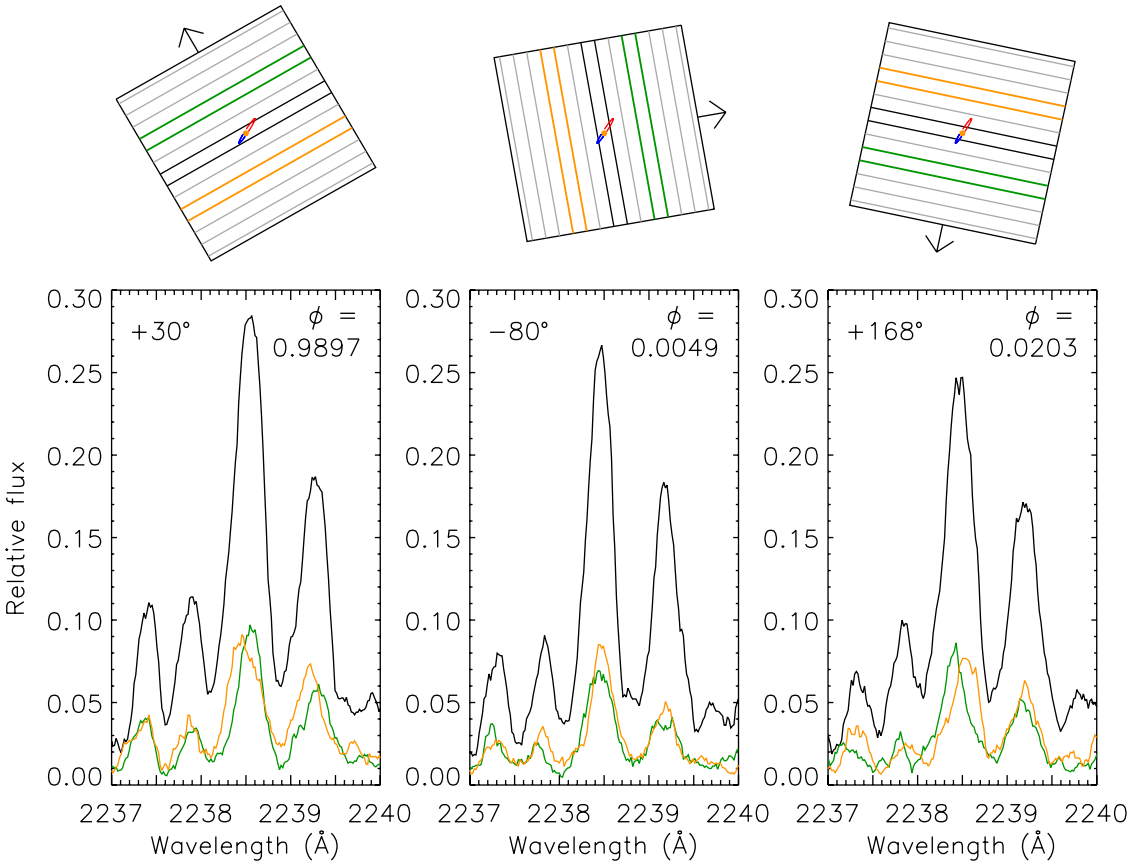

Figure 9. Radial velocity differences. The solid line plots the relative flux extracted from the central row of pixels, the green line plots that extracted from three rows above the central row, and the orange line that from three rows below. Above each of the spectra is a depiction of the aperture and its orientation relative to the orbit. The pixel size in the wavelength direction has been suppressed, and the row of spatial pixels responsible for each of the plotted lines has been outlined in the color with which relative flux from the relevant row was plotted. The portion of the hot component's relative orbit in which it is moving toward us relative to the systemic velocity is plotted in blue, and the portion in which it is moving away is plotted in red. These data were obtained through the $0''.2 \times 0''.2$ aperture at medium spectral resolution on 1997 November 29 ($\phi = 0.9897$), 1998 March 22 ($\phi = 0.0049$), and 1998 July 14 ($\phi = 0.0203$).

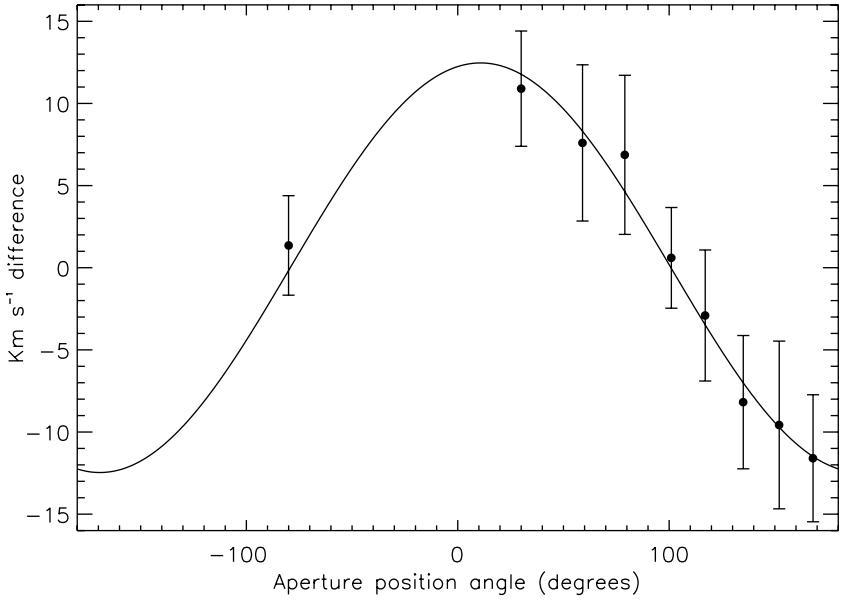

Figure 10. Net velocity structure in the envelope. Filled circles represent the average of the difference between the radial velocity as measured three rows above the central row and that measured three rows below the central row for a sample of 24 high-excitation lines observed at high spectral resolution with the $0.1 \times 0''.2$ aperture, while the hot component was still in eclipse in the NUV. The error bars are one standard deviation of the mean obtained when averaging the 24 lines at each epoch. This velocity difference is correlated with the aperture position angle, and has been fitted with a simple sine curve (solid line).

spatially summed relative flux to erg cm^{-2} s^{-1} Å^{-1}, as long as the conversion is applied over a small enough wavelength range such that the error introduced by intensity variation along the echelle order is minimal.

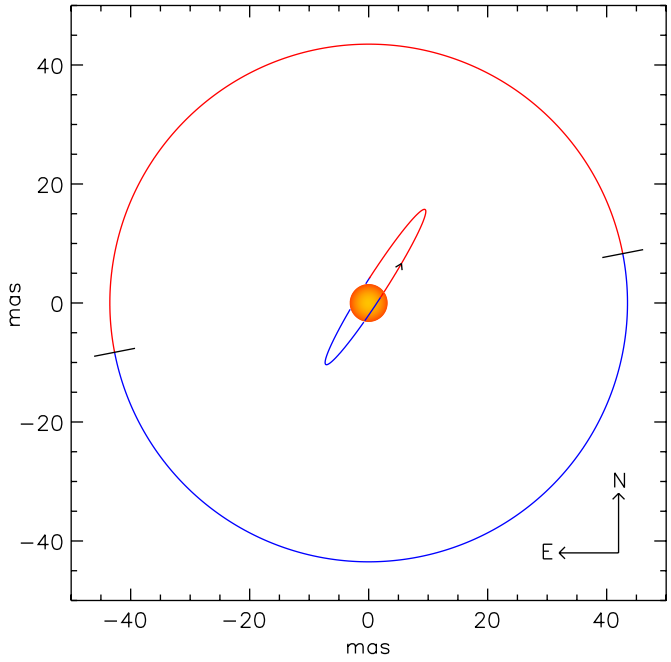

Figure 11. The orientation of the envelope velocity structure. The relative orbit of the hot component and the M supergiant are plotted to scale. Portions of the hot component's orbit in which it is moving toward/away from Earth relative to the systemic velocity are plotted in blue/red respectively. The large circle has a radius of 3 spatial pixels, and the half of the envelope in which the relative motion is toward/away from Earth is also plotted in blue/red respectively.

In order to convert relative flux to erg cm^{-2} s^{-1} Å^{-1}/row, one must know the spatial PSF, which is dependent on both the observed wavelength and the echelle used for the observation. Furthermore, changes in the telescope focus can also change the spatial PSF. It must be empirically determined from a wavelength region within which the flux is believed to arise from a spatially compact region. For VV Cep out of eclipse, the UV continuum, including weak high-excitation absorption and inverse P-Cygni emission likely to form in gas close to the hot component, shows the same spatial distribution (see Figure 7), and was assumed to arise from a point source. For each extended feature that was measured, a region of point-source flux very close in wavelength was identified. The relative flux was summed in each row within this point-source spectral region in order to derive the relevant spatial PSF. With this spatial PSF in hand, one can determine what fraction of the calibrated flux in a point-source wavelength region actually fell on the central row of pixels by taking the ratio of the sum of the relative flux in this wavelength region in the central row to the sum of the relative flux in the central row plus the seven rows on either side. Then relative flux can be converted to erg cm^{-2} s^{-1} Å^{-1}/row and the strength of the extended emission can be compared from one line to another.

It should be noted that the spatial PSF can be derived only for observations made out of eclipse. At midtotality, the emission features we observe may well all form within the extended M supergiant wind, while the emerging blue-shifted emission arising from gas associated with the hot component probably comes from a region more extended than the stellar companion. Little true continuum (which *would* come from an effective point source) is observed during totality. The continuum we do see is strongest at short wavelengths and is believed to arise from Rayleigh scattering in the extended envelope, and thus also does not have a point-source origin. A long-wavelength continuum is believed to arise from the M supergiant photosphere, and could be considered a point source. However, it is relatively faint and appears to be severely affected by scattered light, which produces only a minor contribution out of eclipse.

The flux observed in any HIRES pixel is dependent on both the location in the envelope from which it was emitted and the spatial PSF of the STIS instrument. We assume that all of the flux in row +5 in the point-source wavelength region was emitted from a spatially compact region and fell on row +5 through the spatial PSF. We can therefore scale the relative flux (in erg cm^{-2} s^{-1} Å^{-1} row^{-1}) in the central row of pixels by the empirically determined PSF, and subtract it from the relative flux in row +5, leaving us with a measure of the extended emission. We then sum this difference over the wavelength region included in the emission line profile for 149 lines selected on the basis of being unblended or the strongest contributor to a blend and for having a nearby point-source wavelength region.

The extended flux in row +5 will depend on both the intrinsic brightness of a line and the degree of extension of the emission in the line. It is likely that the extended emission we detect out of eclipse arises from the same gas that produces the emission observed during eclipse. In order to investigate this, we have integrated the flux seen in emission longward of the wind absorption feature for these lines at $\phi = 0.9897$, which was chosen because the observation was made near midtotality, before much gas in the vicinity of the hot component had begun to emerge from eclipse. Only the emission longward of the wind absorption was included because it is only that part of the line profile that is seen as extended.

The sum of the extended flux in row +5 is plotted as a function of the integrated flux in the line during total eclipse in Figure 12. Because our analysis includes lines with wavelengths that range from 2100 to 3100 Å, there will be a significant change in the interstellar reddening over this wavelength range, and the fluxes have been dereddened for an $E(B-V)$ of 0.4 (Hack et al. 1989). All measured lines but those from Fe II are plotted as x's, with Fe II plotted as filled circles or diamonds, color-coded according to the lower-energy level. Error bars have been suppressed in order to avoid confusion, but see Figure 13.

Lines with the lowest excitation potentials (<0.5 eV) are notably weaker than higher-excitation lines. This is the case even for lines with comparable gf values. Strong lower-excitation lines have broader wind absorption, and it is likely that this absorption at least strongly contributes to this effect by eating into the emission. As expected, there is a clear trend: lines with strong emission during total eclipse show strong extended flux out of eclipse. However, there is also a clear dependence on excitation potential, in that the extended flux is weaker for lines with excitation potential greater than 2 eV.

This effect is further seen in Figure 13, in which the ratio of the extended flux to the integrated line flux during totality is plotted against log gf. Only Fe II lines are included in order to exclude abundance and ionization effects. Furthermore, any uncertainties in the reddening correction will cancel. Some features were measurable more than once (up to as many as four times), in different orders either within the same grating setting and/or with different grating settings. Error bars represent the standard deviation of the mean for lines with multiple measurements.

There is only a slight trend for lines with weaker gf values to appear more extended. What is clearly seen in this figure

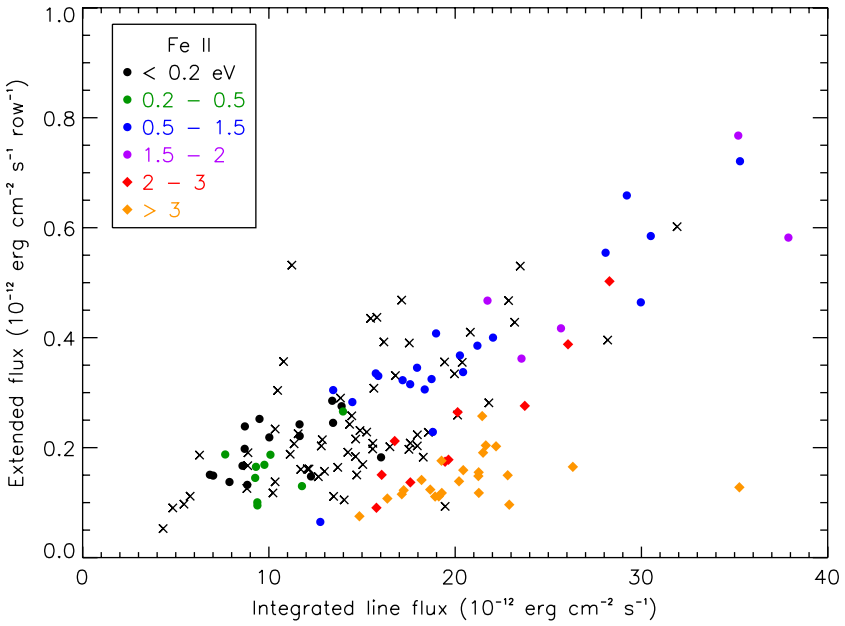

Figure 12. Extended flux vs. integrated flux in totality. The sum of the flux in the fifth row of HIRES pixels above the central row near the first quadrature ($\phi = 0.1712$, 2001 August 8, position angle +146°) is plotted against the integrated flux observed within the line near midtotality ($\phi = 0.9897$, 1997 November 29). All measured lines are plotted with x's, with Fe II also plotted with filled circles color-coded by line excitation potential. All fluxes have been dereddened for an $E(B - V)$ of 0.4. Note the greater degree of extension observed for the lower-excitation lines.

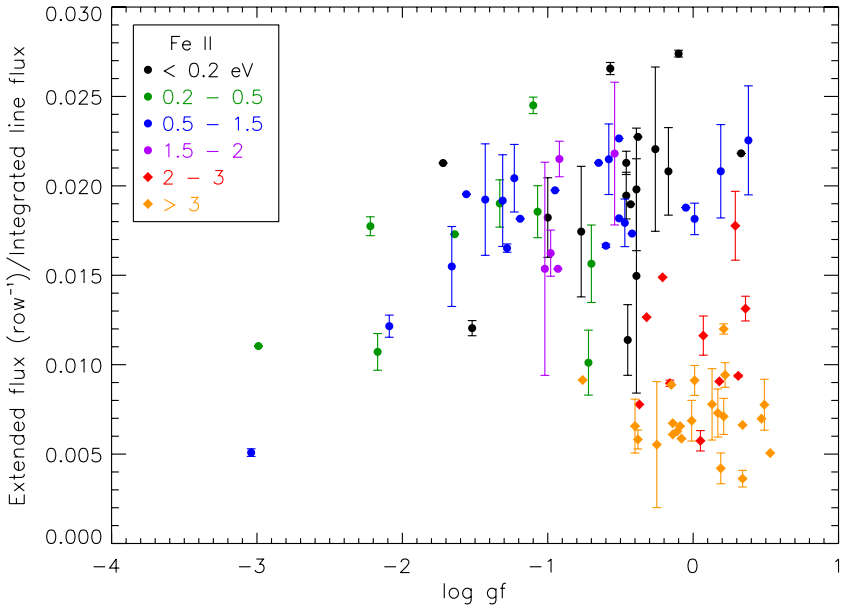

Figure 13. Normalized extended flux vs. log gf. The ratio of the sum of the flux in the fifth row of HIRES pixels above the central row near the first quadrature ($\phi = 0.1712$, 2001 August 8, position angle +146°) divided by the integrated flux observed within the line near midtotality ($\phi = 0.9897$, 1997 November 29) is plotted against log gf. Only Fe II lines are included; they are color-coded with line excitation potential. The greater degree of extension observed for the lower-excitation lines is apparent. Error bars represent the standard deviation of the mean for lines with more than one measurement.

is that the extension is detectable to a much lower gf value for low-excitation lines, and the lower degree of extension for high-excitation lines is even more apparent than in Figure 12.

6. SUMMARY

The eclipsing M2 Iab + B binary system, VV Cep, was observed with *HST*/STIS at 21 epochs from midtotality in 1997 to past the first quadrature in 2003. The echelle spectra were reprocessed in two dimensions using HIRES pixels with a spatial size of 0.″0145. Extended emission beyond that expected for a point source was detected in all 21 observations.

During total eclipse of VV Cep, a rich emission spectrum is observed. Strong low-excitation lines are cut by blue-shifted absorption from the M supergiant wind, resulting in double-peaked emission features. As the hot component approached egress from eclipse, the emission shortward of the wind absorption systematically strengthened, suggesting that it is produced by gas in the vicinity of the hot component. The two-dimensional data confirmed this supposition, as the increasing blue-shifted emission was observed to have a narrower spatial extent than the emission longward of the wind absorption, whose intensity did not change substantially during egress.

After the emergence of the hot component from eclipse, the spectrum is dominated by absorption, with the strongest absorption bottoming out on the emission features that were observed during totality. It is this emission that is spatially extended. The rest of the spectrum, including the hot component's continuum, and inverse P-Cygni emission and high-excitation absorption components believed to form in gas accreting onto the hot component, has a spatial profile consistent with that expected from a point source.

Radial velocity differences across the spatially extended emission have been detected. A sample of lines unaffected by wind absorption were measured for the nine total eclipse observations. The difference between the radial velocity 3 pixels on either side of the center correlated with the aperture position angle and was fitted well with a simple sine curve with an amplitude of 13 km s^{-1}, yielding a net rotation of the gas within the envelope. Three HIRES pixels correspond to $\sim$0.″044 or about 14 M-star radii. Our interpretation is that the M star's wind is "wrapped up" into a spiral outflow by its orbital motion. The plane of the orbit is determined if we assume that this is aligned with the direction of maximum envelope rotation; we find that the orbital plane is oriented from +11° east of north (receding) through −169° (approaching).

Initial attempts at quantifying the extended emission show that the lines with the greatest degree of extension at the first quadrature have about 3% of the line's integrated midtotality flux contained in the fifth row of HIRES pixels to the southeast (with position angle $\sim$140°). Five HIRES pixels correspond to $\sim$0.″073, or $\sim$23 M-star radii.

We would like to thank an anonymous referee for suggestions which have improved the presentation of this paper. P.D.B. and W.H.B. wish to acknowledge support for General Observer Programs GO-7269, 8257, 8779, and 9231, provided by NASA through a grant from the Space Telescope Science Institute, which is operated by the Association of Universities for Research in Astronomy, Inc., under NASA contract NAS 5-26555. P.D.B. also received funding from the National Sciences and Engineering Research Council (NSERC) of Canada in support of a continuing radial velocity program at the Dominion Astrophysical Observatory. W.H.B. acknowledges support from Wellesley College and T.R.G. acknowledges research support from the *HST* Project Office at NASA's Goddard Space Flight Center.

REFERENCES

Bauer, W. H., & Bennett, P. D. 2000, PASP, 112, 31
Bauer, W. H., Bennett, P. D., & Brown, A. 2007, ApJS, 171, 249
Bauer, W. H., Stencel, R. E., & Neff, D. H. 1991, A&AS, 90, 175
Bennett, P. D., Bauer, W. H, & Brown, A. 2002, in ASP Conf. Ser. 260, Interacting Winds from Massive Stars, ed. A. Moffat, & N. St-Louis (San Francisco, CA: ASP), 465
Bennett, P. D., Brown, A., Fawcett, S. M., Yang, S., & Bauer, W. H. 2004, in ASP Conf. Ser. 318, Spectroscopically and Spatially Resolving the Components of Close Binary Stars, ed. R. W. Hilditch, H. Hensberge, & K. Pavlovski (San Francisco, CA: ASP), 222
Cardelli, J. A., Clayton, G. C., & Mathis, J. S. 1988, ApJ, 329, L33
Gawryszczak, A. J., Mikolajewska, J., & Rozyczka, M. 2002, A&A, 385, 205
Gull, T. R., Kober, G. V., & Nielsen, K. E. 2006, ApJS, 163, 173
Hack, M., Engin, S., & Yilmaz, N. 1989, A&A, 225, 143
Hagen, W., Black, J. H., Dupree, A. K., & Holm, A. V. 1980, ApJ, 238, 203
Lejeune, Th., Cuisinier, F., & Buser, R. 1997, A&AS, 125, 229
Mastrodemos, N., & Morris, M. 1998, ApJ, 497, 303
Nagae, T., Oka, K., Matsuda, T., Fujiwara, H., Hachisu, I., & Boffin, H. M. J. 2004, A&A, 419, 335
Quijano, et al. 2007, "STIS Instrument Handbook," Version 8.0 (Baltimore, MD: STSCI), http://www.stsci.edu/hst/stis/documents/handbooks/currentIHB/cover.html, Section 13.6
Theuns, T., & Jorissen, A. 1993, MNRAS, 265, 946
Valenti, J. A., Lindler, D., Bowers, C., Busko, I., & Quijano, J. K. 2002, Instrument Science Report STIS 2002-001 (Baltimore, MD: STScI)
van de Kamp, P. 1977, AJ, 82, 750
Walder, R. 1997, in IAU Colloq. 163, ASP Conf. Ser. 121, Accretion Phenomena and Related Outflows, ed. D. T. Wickramasinghe, G. V. Bicknell, & L. Ferrario (San Francisco, CA: ASP), 822
Wright, K. O. 1977, JRASC, 71, 152